THE JOURNAL OF PHYSICAL CHEMISTRY Letters

Letter

pubs.acs.org/JPCL

Imaging Charge Transfer State Excitations in Polymer/Fullerene Solar Cells with Time-Resolved Electrostatic Force Microscopy

Phillip A. Cox, Micah S. Glaz, Jeffrey S. Harrison, Samuel R. Peurifoy,[§] David C. Coffey,[δ] and David S. Ginger*

Department of Chemistry, University of Washington, Seattle, Washington 98195, United States

Supporting Information

ABSTRACT: We demonstrate nanoscale imaging of charge transfer state photoexcitations in polymer/fullerene bulk heterojunction solar cells using time-resolved electrostatic force microscopy (trEFM). We compare local trEFM charging rates and external quantum efficiencies (EQE) for both above-gap and below-gap excitation of the model system poly[2-methoxy-5-(3′,7′-dimethyloctyloxy)-1,4-phenylenevinylene] (MDMO-PPV) and [6,6]-phenyl C_{61} butyric acid methyl ester (PCBM). We show that the local trEFM charging rate correlates with device EQE for both above-gap and below-gap photoexcitation, demonstrating that EFM methods have sufficient sensitivity to detect the low EQEs associated with CT state formation, a result that could be useful for probing weak subgap excitations in nanostructured materials such as quantum dot and organometal halide perovskite solar cells. Further, we use trEFM to map spatial variations in EQE arising from subgap CT excitation in organic photovoltaics (OPVs) and find that the local distribution of photocurrent arising from these states is nearly identical to the spatial variation in EQE from above-gap singlet excitation. These results are consistent with recent work showing that both above-gap and below-gap excitation have similar internal quantum efficiency.

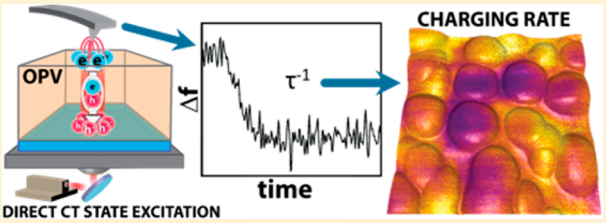

Organic photovoltaics (OPVs) offer many potential advantages as a next-generation thin-film solar technology. They have been demonstrated with over 10% power conversion efficiencies,[1,2] are made from inherently earth-abundant and nontoxic materials, can be processed from greener, nonhalogenated solvents,[3,4] and accelerated stability testing has predicted lifetimes exceeding seven years.[5] Furthermore, there is seemingly still room to improve overall performance, as a number of studies have estimated that the ultimate power conversion efficiency limits for OPVs should be in the range of 20−27%.[6,7]

However, continued improvements in OPV performance will require better understanding of the fundamental recombination loss mechanisms taking place in organic semiconductors.[7] Currently, the most efficient OPVs comprise a donor and acceptor material arranged in a bulk heterojunction morphology that has a profound effect on charge generation, recombination, transport, and hence device efficiency.[8−10] In addition, many authors have identified the charge transfer (CT) state that forms at the donor/acceptor interface as having a key influence on device performance.[7,11−15] For instance, the V_{oc} of organic solar cells shows a strong empirical correlation with the energy of the CT state.[16−19]

Because of the importance of morphology, there has been a great deal of work both to characterize the structure of polymer/fullerene blends, as well as to develop methods that can correlate local morphology with local variations in device performance.[20−27] Likewise, researchers have used a wide range of optical spectroscopic probes and device measurement techniques to characterize the energetics and kinetics of subgap CT states in OPV blends,[12,28−32] as well as subgap excitations in related nanostructured solar materials, such as quantum dot solar cells[33,34] and organometal halide perovskites.[35] Despite the large body of work demonstrating substantial spatial heterogeneity in charge generation, recombination, and transport associated with above-gap photoexcitation of OPV blends,[36−43] performing similar experiments to map spatial variations in CT state photocurrents is challenging because of the extremely small EQEs (10^{-3}−10^{-6} or lower) associated with exciting the weakly allowed CT transition. Indeed, measuring photocurrents from CT states in macroscopic devices typically requires sensitive lock-in[31] or Fourier-Transform Photocurrent Spectroscopy methods.[30,44]

Here we demonstrate that time-resolved electrostatic force microscopy (trEFM)[23,25,45] can be used to map local variations in EQE across the solar spectrum, including direct subgap excitation of the CT state. We compare trEFM maps taken with above- and below-gap excitation and show that, while morphology influences local variations in carrier generation and collection, excitation wavelength does not.

trEFM is a noncontact atomic force microscopy (AFM) technique that measures capacitive force gradients and surface

Received: June 25, 2015
Accepted: July 6, 2015
Published: July 6, 2015

DOI: 10.1021/acs.jpclett.5b01360
J. Phys. Chem. Lett. 2015, 6, 2852−2858

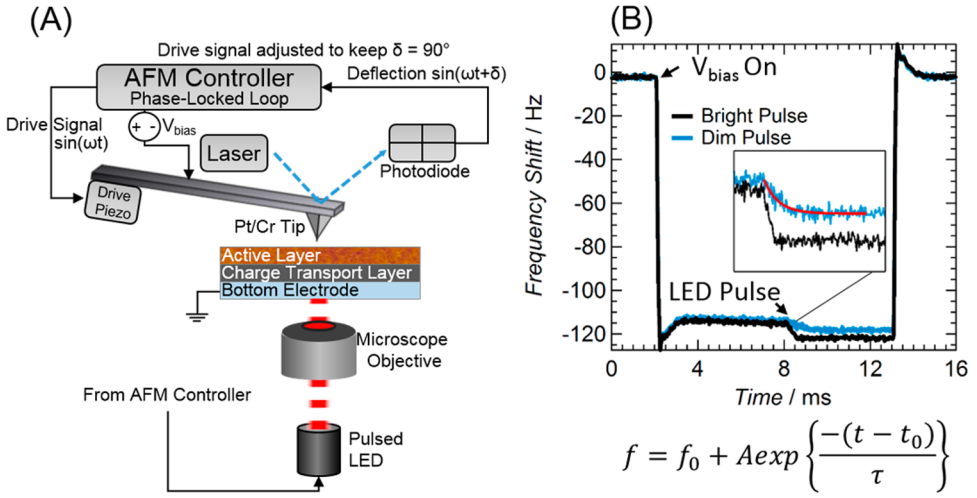

Figure 1. (A) Schematic of the time-resolved electrostatic force microscopy technique. (B) A raw data trace plotting cantilever frequency shift versus time during a measurement cycle at a single pixel as the measurement voltage and then illumination are turned on. We fit the frequency shift versus time after the LED pulse to the exponential decay (red trace) function shown, where the inverse of tau is characteristic of the local photocharging rate of the tip−sample junction, a value that is proportional to local EQE.

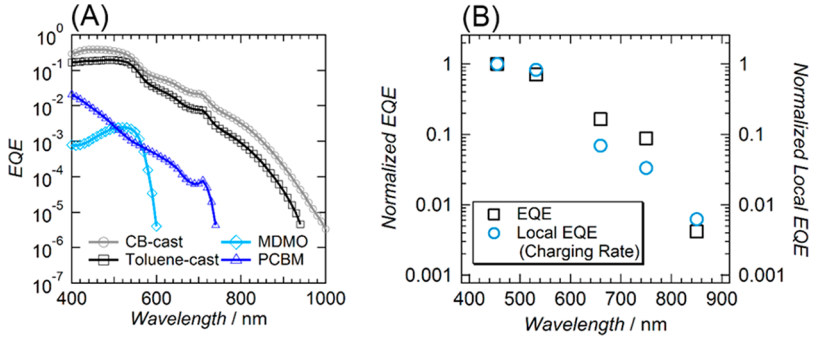

Figure 2. (A) Lock-in amplifier-detected EQE of neat MDMO-PPV, neat PCBM, 1:4 MDMO-PPV:PCBM blend cast from chlorobenzene, and 1:4 MDMO-PPV:PCBM cast from toluene. (B) Comparison between bulk device EQE and photon-flux normalized trEFM charging rates (local EQE) as a function of wavelength for a device cast from chlorobenzene.

potentials between the sample and a conductive AFM cantilever.[23,24] Noncontact scanning probe methods like trEFM are useful for imaging soft samples as they greatly reduce the chance of damaging both the cantilever tip and thin film components, enabling repeated imaging of the same area under various conditions. As such, we have previously used trEFM to assess the role of morphology on both performance and photochemical damage in organic photovoltaics and we have demonstrated that photoinduced charging rates in trEFM are proportional to the external quantum efficiency of bulk devices under a range of conditions in model polymer/polymer blends.[23,25,45]

Figure 1A shows a schematic of the trEFM setup we used for probing subgap CT excitation. Briefly, we photoexcite a partially completed polymer/fullerene solar cell through the transparent bottom substrate (indium tin oxide coated glass) with a short (4 ms) LED pulse that creates charge carriers in the active layer. A positive bias on the AFM cantilever causes negative charge carriers to move toward the sample surface, and these carriers lead to a decrease in the resonance frequency of the AFM cantilever.[46,47] By tracking the frequency as a function of time, we can thus determine how rapidly the photoinduced carrier population builds up at the film surface under the AFM tip. The experiment essentially measures the time it takes to charge the tip−sample capacitor with the local photocurrent generated under the tip. The rise times are thus associated with the magnitude of the local EQE/photocurrent (*not* the exciton dissociation event itself, which typically occurs on femtosecond scales[29,48] in these materials).

Figure 1B shows a raw data trace of a single pixel in an image during the trEFM measurement cycle for two different light intensities. The rise time of interest is the one following the LED pulse as indicated in the figure. In this example, the tip−sample junction charges faster with a brighter pulse. However, for a constant light intensity, local variations in EQE lead to variation in the charging rate between pixels.[23] A trEFM image is generated by plotting the inverse tau from an exponential decay fit taken at each pixel location.

In this study we use the model system poly[2-methoxy-5-(3′,7′-dimethyloctyloxy)-1,4-phenylenevinylene] (MDMO-PPV):[6,6]-phenyl C_{61} butyric acid methyl ester (PCBM). The film morphology of this blend is easily tailored by choice of casting solvent,[8] and both the morphology and charge transfer state properties of MDMO-PPV:PCBM devices have been studied in detail,[8,11,49] making it an ideal system to test the ability of trEFM to resolve charge carriers arising from both above- and below-gap photoexcitation.

Figure 2A shows the lock-in detected external quantum efficiencies of macroscopic solar cells made from neat MDMO-PPV, neat PCBM, and blends of the two materials in a 1:4 wt/

DOI: 10.1021/acs.jpclett.5b01360
J. Phys. Chem. Lett. 2015, 6, 2852−2858

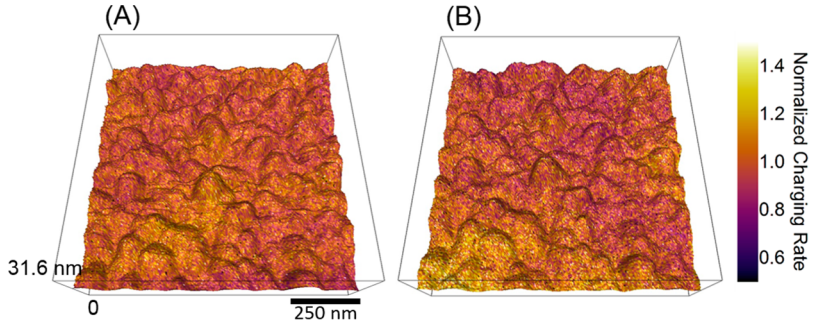

Figure 3. (A) Normalized singlet state charging rate (532 nm LED) and (B) CT state charging rate (850 nm LED with 850 nm long-pass filter) overlaid on film topography of a 1:4 MDMO-PPV:PCBM film cast from chlorobenzene.

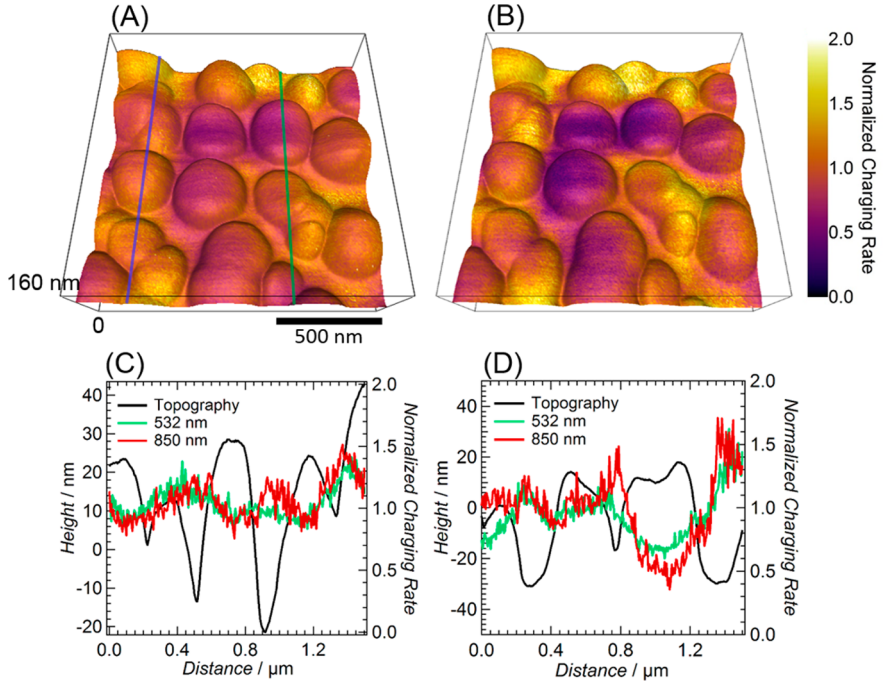

Figure 4. (A) Normalized singlet state charging rate (532 nm LED) and (B) CT state charging rate (850 nm LED with 850 nm long-pass filter) overlaid on film topography of a 1:4 MDMO-PPV:PCBM film cast from toluene. (C) and (D) Line traces of topography height and charging rates at both 532 and 850 nm excitation taken at the blue (C) and green (D) lines shown in (A).

wt ratio cast from both chlorobenzene and toluene. The pure MDMO-PPV alone shows an EQE peak around ∼550 nm before sharply dropping off by 600 nm, while PCBM exhibits a longer tail but drops off steeply at 750 nm. As expected, the MDMO-PPV:PCBM blends show higher overall EQEs that resemble a superposition of the MDMO-PPV and PCBM spectra at shorter wavelengths, but include a broad red tail in the near IR.[11] This subgap EQE tail is broader than the sum of the individual components, and arises due to subgap excitation directly into the interfacial CT states comprising an electron on a fullerene and a hole on the MDMO-PPV.[8]

We have previously shown that the trEFM charging rates correlate well with EQE for both pristine and photo-oxidized films.[23,45] Here we explore whether this relationship holds true for photocarriers generated via subgap excitation of CT states by comparing the wavelength-dependence of the device EQE and trEFM charging rate. Figure 2B (blue circles) plots the wavelength-dependent, photon-flux normalized trEFM charging rates measured on an MDMO-PPV:PCBM blend cast from chlorobenzene. Figure 2B also plots the device EQEs measured at the same wavelengths (see Supporting Figure S1 and S2). The close agreement between the traces for the device EQE and the trEFM charging rates as they both change by over 2 orders of magnitude as the wavelength changes from 455 to 850 nm shows that trEFM can indeed be used to map local EQEs, even for direct excitation of subgap CT states. While the EQE for this CB blend is ∼0.1% (10^{-3}) at 850 nm, we can use trEFM to measure down to levels as low as 0.001% (10^{-5}) (Supporting Figure S6). Recording a local subgap photocurrent with conventional photoconductive AFM would require measurement of attoAmpere level currents. This level of detection is made possible by the sensitivity of EFM methods to local force gradients: under favorable conditions, sensitivity to single charges is even possible.[50]

Figure 3A,B shows charging rate images taken at 532 and 850 nm excitation overlaid on AFM topography of a 1:4 MDMO-PPV:PCBM film cast from chlorobenzene (frequency shift images included in Supporting Information Figure S4). The morphology consists of small features on the order of 30−60 nm with a relatively smooth surface roughness. Figure 3A shows a typical charging rate map where the sample was photoexcited with a 532 nm LED. We normalized this image

DOI: 10.1021/acs.jpclett.5b01360
J. Phys. Chem. Lett. 2015, 6, 2852−2858

(and all subsequent images presented here), by dividing every pixel by the average charging rate. This process highlights spatial variations relative to the film average. However, for both above- and below-gap excitation, we find little to no local variation in charging rate for films cast from chlorobenzene, regardless of excitation wavelength or local morphology. This lack of observable variation is expected given the very small scale of the features in a chlorobenzene-cast MDMO-PPV:PCBM blend. To explore spatial variations in photocurrent collection more easily as a function of wavelength, we next turn to examine blends spin-coated from toluene.

Figure 4A,B shows trEFM charging rate images taken at 532 and 850 nm overlaid on the AFM topography for a 1:4 MDMO-PPV:PCBM film cast from toluene (frequency shift images included in Supporting Information Figure S3). This blend forms films consisting of large aggregates, roughly 250−500 nm in diameter, separated by flat valleys. The structure of MDMO-PPV:PCBM devices cast from toluene has been meticulously studied and reported elsewhere.[8,51,52] Briefly, the large aggregates are PCBM domains, which can be covered with a mixed MDMO-PPV:PCBM capping layer. The valleys are regions of mixed MDMO-PPV and PCBM. For above-gap photoexcitation, charging mainly occurs in between, and at the edges of fullerene aggregates, as well as on top of some of the aggregates. These locations are where there is the most polymer, which is responsible for most absorption at 532 nm. Photoconductive-AFM (pcAFM) measurements show that current collection mainly occurs at the aggregate boundaries but not in the flat, mixed domains.[36] While the structure and overall charging rate trends in these trEFM images are generally consistent with pcAFM on the same films, the trEFM images show subtle differences that we attribute to the ability of trEFM to detect and resolve photocurrent variations in the areas between fullerene aggregates, a result that is difficult to achieve with contact-mode pcAFM (see Supporting Information Figure S7).

Figure 4B shows similar charging rate images obtained by exciting only the CT state with an 850 nm LED and 850 nm long-pass filter. Surprisingly, the trEFM images in Figure 4A,B are very similar, despite being taken at very different excitation energies. Notably, the line traces shown in Figure 4C,D show virtually the same spatial variation with small deviations. We attribute the small observed deviations to the result of random noise associated with measuring what is the equivalent of attoAmpere level currents. We provide additional analysis and discussion in Supporting Information Figure S8, showing that the correlation between the images taken with above-gap and below-gap excitation is as high as can be expected between successive AFM scans under these experimental conditions and imperfect spatial matching. We thus take the strong correlation between the two images to be evidence that the local distribution of EQEs is insensitive to excitation wavelength as explained below.

At first, it may seem unexpected that the EQE maps taken at 532 and 850 nm excitation show the same spatial structure. If we *had* observed structure in the trEFM maps that differed systematically between above-gap (excitonic) and below-gap (CT state) excitation as a function of position, it would imply that either the local absorption varies due to local composition or that the local yield of free carriers per absorbed photon (internal quantum efficiency, IQE) changed from region to region depending on excitation wavelength. On the other hand, the lack of change in structure upon change in wavelength implies that either (A) the features at 532 and 850 nm share both the same spatial variations in absorption and charge separation (IQE), or (B) the local variations in absorption and IQE are coincidentally inversely proportional everywhere so as to exactly cancel (further discussion provided in Supporting Information Section 9). Since the excitonic (above-gap) and charge transfer state (below-gap) absorptions both involve MDMO-PPV, and it is known that the MDMO-PPV phases contain molecularly dispersed PCBM,[8,53] it seems reasonable that both excitonic and CT absorption track MDMO-PPV concentration in this blend. Therefore, we conclude that the probability of forming charge carriers from an absorbed photon must be essentially equal at above- and below-gap photoexcitation. If this was not the case, then to preserve the local distribution in EQEs between singlet and CT excitation, the IQE and EQE would have to coincidentally anticorrelate everywhere in the film. Due to the unlikeliness of this possibility, we propose that IQE is independent of excitation wavelength.

Notably, Vandewal et al.[12] recently reported that the internal quantum efficiency (IQE) of a number of polymer/fullerene blends (including MEH-PPV, a polymer closely related to MDMO-PPV) is independent of excitation wavelength. Although we emphasize that our trEFM measurements probe EQE, not IQE, we still conclude that the strong correlation between the EQE maps at above- and below-gap excitation shown in Figure 3 and 4 are local evidence consistent with the findings of Vandewal and co-workers. In other words, the only likely way to have the macroscopic IQE be the same at two different wavelengths in a sample with significant spatial heterogeneity is if the microscopic variations in IQE are also independent of excitation wavelength.

We have employed time-resolved electrostatic force microscopy to acquire nanoscale images of the charge-transfer state in MDMO-PPV:PCBM solar cells. Over the range of the solar spectrum, even at sub-bandgap wavelengths, we find that the charging rates from trEFM point scans are proportional to the EQE of a bulk device, demonstrating that trEFM can be used as a local probe for EQE, even for very weakly absorbing states, with EQEs as low as 10^{-5}. The high sensitivity of trEFM to local carrier generation makes it ideal for dynamic characterization of a broad range of nanostructured materials, such as intermediate band quantum dot solar cells and singlet fission solar cells where carriers generated from weak subgap excitations are of interest. For heterogeneous OPV device morphologies, we found that the charging rates for both above- and below-gap photoexcitation are fastest in areas where MDMO-PPV and PCBM are well mixed, with the slowest charging rates occurring in the pure PCBM phase. These results provide local evidence in support of recent work suggesting that IQE is insensitive to excitation wavelength.

■ EXPERIMENTAL SECTION

Device Preparation. Precoated ITO slides (Thin Film Devices, Inc.) were sonicated in sequential solutions of acetone and isopropanol for 20 min each and then dried with nitrogen. The substrates were plasma-cleaned for 5 min and then immediately spin-coated with a ∼30 nm layer of PEDOT:PSS (Clevios P VP 4083 Al, H.C. Stark Chemicals) before annealing at 150 °C for 20 min under dry nitrogen. MDMO-PPV (synthesized by Lee Park's group, Williams College)[54] and PCBM (nano-c) solutions were created separately in either toluene or chlorobenzene solvent and stirred overnight at 60 °C. In a

DOI: 10.1021/acs.jpclett.5b01360
J. Phys. Chem. Lett. 2015, 6, 2852−2858

nitrogen glovebox, 80 μL of 1:4 wt/wt MDMO-PPV:PCBM solution was spin-coated onto the PEDOT:PSS layer to a thickness of ∼85 nm. For films used in EQE measurements, 80 nm aluminum contacts were thermally evaporated onto the active layer through a shadow mask.

Device Testing. External quantum efficiency measurements were performed with a monochromated (Acton Research Corporation Microspec 2300i) 250 W lamp (Princeton Instruments), sourcemeter (Keithley 2400), lock-in amplifier (Stanford Research Systems SR830) and calibrated Si photodiode (OSI-Optoelectronics). A device mask ensured the same 0.0122 cm^2 of light exposure to all devices and the photodiode.

Atomic Force Microscopy. AFM measurements were carried out on an Asylum Research MFP-3D Bio atomic force microscope on top of an inverted Nikon Eclipse Ti microscope and Table Stable vibration isolation stage. 75 kHz resonance frequency BudgetSensor silicon cantilevers with a Pt/Cr conductive coating were used. Devices were sealed from the environment in an Asylum Research closed flow cell with a constant stream of dry nitrogen. Excitation light sources were LEDEngin 455, 532, 660, 750, and 850 nm LZ4-series LEDs. The LEDs were attached to a side input of the microscope where they were reflected off one full mirror and then a 50/50 beam splitter (850 used a full mirror) filter cube before going through a 40x Nikon Pan Flour objective. For CT-excitation images, an 850 nm long-pass filter (ThorLabs FEL0850) was used in front of the 850 nm LED to ensure no singlet state excitation (see Supporting Information Figure S5). In comparing macroscopic EQE to local trEFM measurements, the macroscopic EQEs were weighted to the emission spectra of the LEDs used in the trEFM measurements (see Supporting Information Figure S1). All trEFM images are 256 × 256 pixels with 10 averages per pixel and fit to the Igor software's built-in exponential decay function with realistic constraints for the time constant. All trEFM imaging and analysis was carried out with our custom Igor code operating within the Asylum Research AFM software.

■ ASSOCIATED CONTENT

Supporting Information

Figure S1: LED Spectra and Si diode responsivity used in EQE adjustments for Figure 2B. Figure S2: Point scans of 1:4 MDMO-PPV:PCBM cast from chlorobenzene at various wavelengths and intensities used in Figure 2B. Figure S3: Frequency shift images of a 1:4 MDMO-PPV:PCBM film cast from toluene. Figure S4: Frequency shift images of a 1:4 MDMO-PPV:PCBM cast from chlorobenzene. Figure S5: MDMO-PPV and PCBM neat trEFM points scans at 455 and 850 nm excitation. Figure S6: Lower limits of trEFM resolution obtained by scans and EQE of MDMO-PPV with incremental additions of PCBM by wt/wt %. Figure S7: Comparison between photoconductive-AFM and trEFM images of a 1:4 MDMO-PPV:PCBM film cast from toluene. Figure S8: Correlation scatter plots and discussion. Section 9: Additional discussion of IQE dependence on excitation wavelength. The Supporting Information is available free of charge on the ACS Publications website at DOI: 10.1021/acs.jpclett.5b01360.

■ AUTHOR INFORMATION

Corresponding Author

*E-mail: ginger@chem.washington.edu.

Present Addresses

[§](S.R.P.) Department of Chemistry, University of Miami, Coral Gables, Florida, 33146, United States

[δ](D.C.C.) Department of Chemistry and Physics, Warren Wilson College, Swannanoa, North Carolina 28778, United States

Notes

The authors declare no competing financial interest.

■ ACKNOWLEDGMENTS

This work was completed under NSF DMR-1306079. The authors thank Dr. David Moerman for helpful discussions.

■ REFERENCES

(1) You, J.; Dou, L.; Yoshimura, K.; Kato, T.; Ohya, K.; Moriarty, T.; Emery, K.; Chen, C.; Gao, J.; Li, G.; et al. A Polymer Tandem Solar Cell with 10.6% Power Conversion Efficiency. *Nat. Commun.* **2013**, *4*, 1446.

(2) Liu, Y.; Zhao, J.; Li, Z.; Mu, C.; Ma, W.; Hu, H.; Jiang, K.; Lin, H.; Ade, H.; Yan, H. Aggregation and Morphology Control Enables Multiple Cases of High-Efficiency Polymer Solar Cells. *Nat. Commun.* **2014**, *5*, 5293.

(3) Chen, K.-S.; Yip, H.-L.; Schlenker, C. W.; Ginger, D. S.; Jen, A. K. Y. Halogen-Free Solvent Processing for Sustainable Development of High Efficiency Organic Solar Cells. *Org. Electron.* **2012**, *13*, 2870−2878.

(4) Chueh, C.-C.; Yao, K.; Yip, H.-L.; Chang, C.-Y.; Xu, Y.-X.; Chen, K.-S.; Li, C.-Z.; Liu, P.; Huang, F.; Chen, Y.; et al. Non-Halogenated Solvents for Environmentally Friendly Processing of High-Performance Bulk-Heterojunction Polymer Solar Cells. *Energy Environ. Sci.* **2013**, *6*, 3241−3248.

(5) Peters, C. H.; Sachs-Quintana, I. T.; Kastrop, J. P.; Beaupré, S.; Leclerc, M.; McGehee, M. D. High Efficiency Polymer Solar Cells with Long Operating Lifetimes. *Adv. Energy Mater.* **2011**, *1*, 491−494.

(6) Giebink, N. C.; Wiederrecht, G. P.; Wasielewski, M. R.; Forrest, S. R. Thermodynamic Efficiency Limit of Excitonic Solar Cells. *Phys. Rev. B: Condens. Matter Mater. Phys.* **2011**, *83*, 195326.

(7) Koster, L. J. A.; Shaheen, S. E.; Hummelen, J. C. Pathways to a New Efficiency Regime for Organic Solar Cells. *Adv. Energy Mater.* **2012**, *2*, 1246−1253.

(8) Hoppe, H.; Sariciftci, N. S. Morphology of Polymer/Fullerene Bulk Heterojunction Solar Cells. *J. Mater. Chem.* **2006**, *16*, 45−61.

(9) Brabec, C. J.; Gowrisanker, S.; Halls, J. J.; Laird, D.; Jia, S.; Williams, S. P. Polymer-Fullerene Bulk-Heterojunction Solar Cells. *Adv. Mater.* **2010**, *22*, 3839−3856.

(10) Thompson, B. C.; Frechet, J. M. J. Organic Photovoltaics - Polymer-Fullerene Composite Solar Cells. *Angew. Chem., Int. Ed.* **2008**, *47*, 58−77.

(11) Vandewal, K.; Gadisa, A.; Oosterbaan, W. D.; Bertho, S.; Banishoeib, F.; Van Severen, I.; Lutsen, L.; Cleij, T. J.; Vanderzande, D.; Manca, J. V. The Relation between Open-Circuit Voltage and the Onset of Photocurrent Generation by Charge-Transfer Absorption in Polymer: Fullerene Bulk Heterojunction Solar Cells. *Adv. Funct. Mater.* **2008**, *18*, 2064−2070.

(12) Vandewal, K.; Albrecht, S.; Hoke, E. T.; Graham, K. R.; Widmer, J.; Douglas, J. D.; Schubert, M.; Mateker, W. R.; Bloking, J. T.; Burkhard, G. F.; et al. Efficient Charge Generation by Relaxed Charge-Transfer States at Organic Interfaces. *Nat. Mater.* **2014**, *13*, 63−68.

(13) Maurano, A.; Hamilton, R.; Shuttle, C. G.; Ballantyne, A. M.; Nelson, J.; O'Regan, B.; Zhang, W.; McCulloch, I.; Azimi, H.; Morana, M.; et al. Recombination Dynamics as a Key Determinant of Open Circuit Voltage in Organic Bulk Heterojunction Solar Cells: A Comparison of Four Different Donor Polymers. *Adv. Mater.* **2010**, *22*, 4987−92.

(14) Rao, A.; Chow, P. C. Y.; Gelinas, S.; Schlenker, C. W.; Li, C.-Z.; Yip, H.-L.; Jen, A. K. Y.; Ginger, D. S.; Friend, R. H. The Role of Spin

DOI: 10.1021/acs.jpclett.5b01360
J. Phys. Chem. Lett. 2015, 6, 2852−2858

in the Kinetic Control of Recombination in Organic Photovoltaics. *Nature* **2013**, *500*, 435−439.
(15) Schlenker, C. W.; Chen, K.-S.; Yip, H.-L.; Li, C.-Z.; Bradshaw, L. R.; Ochsenbein, S. T.; Ding, F.; Li, X. S.; Gamelin, D. R.; Jen, A. K. Y.; et al. Polymer Triplet Energy Levels Need Not Limit Photocurrent Collection in Organic Solar Cells. *J. Am. Chem. Soc.* **2012**, *134*, 19661−19668.
(16) Vandewal, K.; Tvingstedt, K.; Gadisa, A.; Inganas, O.; Manca, J. V. On the Origin of the Open-Circuit Voltage of Polymer-Fullerene Solar Cells. *Nat. Mater.* **2009**, *8*, 904−909.
(17) Vandewal, K.; Tvingstedt, K.; Gadisa, A.; Inganäs, O.; Manca, J. V. Relating the Open-Circuit Voltage to Interface Molecular Properties of Donor:Acceptor Bulk Heterojunction Solar Cells. *Phys. Rev. B: Condens. Matter Mater. Phys.* **2010**, *81*, 125204.
(18) Piersimoni, F.; Chambon, S.; Vandewal, K.; Mens, R.; Boonen, T.; Gadisa, A.; Izquierdo, M.; Filippone, S.; Ruttens, B.; D'Haen, J.; et al. Influence of Fullerene Ordering on the Energy of the Charge-Transfer State and Open-Circuit Voltage in Polymer:Fullerene Solar Cells. *J. Phys. Chem. C* **2011**, *115*, 10873−10880.
(19) Rand, B. P.; Burk, D. P.; Forrest, S. R. Offset Energies at Organic Semiconductor Heterojunctions and Their Influence on the Open-Circuit Voltage of Thin-Film Solar Cells. *Phys. Rev. B: Condens. Matter Mater. Phys.* **2007**, *75*, 115327.
(20) Brenner, T. J. K.; McNeill, C. R. Spatially Resolved Spectroscopic Mapping of Photocurrent and Photoluminescence in Polymer Blend Photovoltaic Devices. *J. Phys. Chem. C* **2011**, *115*, 19364−19370.
(21) Luria, J. L.; Hoepker, N.; Bruce, R.; Jacobs, A. R.; Groves, C.; Marohn, J. A. Marohn. Spectroscopic Imaging of Photopotentials and Photoinduced Potential Fluctuations in a Bulk Heterojunction Solar Cell Film. *ACS Nano* **2012**, *6*, 9392−9401.
(22) Cox, P. A.; Waldow, D. A.; Dupper, T. J.; Jesse, S.; Ginger, D. S. Mapping Nanoscale Variations in Photochemical Damage of Polymer/Fullerene Solar Cells with Dissipation Imaging. *ACS Nano* **2013**, *7*, 10405−10413.
(23) Coffey, D. C.; Ginger, D. S. Time-Resolved Electrostatic Force Microscopy of Polymer Solar Cells. *Nat. Mater.* **2006**, *5*, 735−740.
(24) Giridharagopal, R.; Rayermann, G. E.; Shao, G.; Moore, D. T.; Reid, O. G.; Tillack, A. F.; Masiello, D. J.; Ginger, D. S. Submicrosecond Time Resolution Atomic Force Microscopy for Probing Nanoscale Dynamics. *Nano Lett.* **2012**, *12*, 893−898.
(25) Reid, O. G.; Rayermann, G. E.; Coffey, D. C.; Ginger, D. S. Imaging Local Trap Formation in Conjugated Polymer Solar Cells: A Comparison of Time-Resolved Electrostatic Force Microscopy and Scanning Kelvin Probe Imaging†. *J. Phys. Chem. C* **2010**, *114*, 20672−20677.
(26) Wong, C. Y.; Penwell, S. B.; Cotts, B. L.; Noriega, R.; Wu, H.; Ginsberg, N. S. Revealing Exciton Dynamics in a Small-Molecule Organic Semiconducting Film with Subdomain Transient Absorption Microscopy. *J. Phys. Chem. C* **2013**, *117*, 22111−22122.
(27) Balke, N.; Maksymovych, P.; Jesse, S.; Kravchenko, I. I.; Li, Q.; Kalinin, S. V. Exploring Local Electrostatic Effects with Scanning Probe Microscopy: Implications for Piezoresponse Force Microscopy and Triboelectricity. *ACS Nano* **2014**, *8*, 10229−10236.
(28) Bakulin, A. A.; Rao, A.; Pavelyev, V. G.; van Loosdrecht, P. H. M.; Pshenichnikov, M. S.; Niedzialek, D.; Cornil, J.; Beljonne, D.; Friend, R. H. The Role of Driving Energy and Delocalized States for Charge Separation in Organic Semiconductors. *Science* **2012**, *335*, 1340−1344.
(29) Gélinas, S.; Rao, A.; Kumar, A.; Smith, S. L.; Chin, A. W.; Clark, J.; van der Poll, T. S.; Bazan, G. C.; Friend, R. H. Ultrafast Long-Range Charge Separation in Organic Semiconductor Photovoltaic Diodes. *Science* **2014**, *343*, 512−516.
(30) Vandewal, K.; Goris, L.; Haeldermans, I.; Nesládek, M.; Haenen, K.; Wagner, P.; Manca, J. V. Fourier-Transform Photocurrent Spectroscopy for a Fast and Highly Sensitive Spectral Characterization of Organic and Hybrid Solar Cells. *Thin Solid Films* **2008**, *516*, 7135−7138.
(31) Street, R. A.; Hawks, S. A.; Khlyabich, P. P.; Li, G.; Schwartz, B. J.; Thompson, B. C.; Yang, Y. Electronic Structure and Transition Energies in Polymer−Fullerene Bulk Heterojunctions. *J. Phys. Chem. C* **2014**, *118*, 21873−21883.
(32) Coffey, D. C.; Larson, B. W.; Hains, A. W.; Whitaker, J. B.; Kopidakis, N.; Boltalina, O. V.; Strauss, S. H.; Rumbles, G. An Optimal Driving Force for Converting Excitons into Free Carriers in Excitonic Solar Cells. *J. Phys. Chem. C* **2012**, *116*, 8916−8923.
(33) Martí, A.; Antolín, E.; Stanley, C. R.; Farmer, C. D.; López, N.; Díaz, P.; Cánovas, E.; Linares, P. G.; Luque, A. Production of Photocurrent Due to Intermediate-to-Conduction-Band Transitions: A Demonstration of a Key Operating Principle of the Intermediate-Band Solar Cell. *Phys. Rev. Lett.* **2006**, *97*, 247701.
(34) Elborg, M.; Noda, T.; Mano, T.; Jo, M.; Sakuma, Y.; Sakoda, K.; Han, L. Voltage Dependence of Two-Step Photocurrent Generation in Quantum Dot Intermediate Band Solar Cells. *Sol. Energy Mater. Sol. Cells* **2015**, *134*, 108−113.
(35) Leijtens, T.; Stranks, S. D.; Eperon, G. E.; Lindblad, R.; Johansson, E. M. J.; McPherson, I. J.; Rensmo, H.; Ball, J. M.; Lee, M. M.; Snaith, H. J. Electronic Properties of Meso-Superstructured and Planar Organometal Halide Perovskite Films: Charge Trapping, Photodoping, and Carrier Mobility. *ACS Nano* **2014**, *8*, 7147−7155.
(36) Coffey, D. C.; Reid, O. G.; Rodovsky, D. B.; Bartholomew, G. P.; Ginger, D. S. Mapping Local Photocurrents in Polymer/Fullerene Solar Cells with Photoconductive Atomic Force Microscopy. *Nano Lett.* **2007**, *7*, 738−744.
(37) Pingree, L. S. C.; Reid, O. G.; Ginger, D. S. Imaging the Evolution of Nanoscale Photocurrent Collection and Transport Networks During Annealing of Polythiophene/Fullerene Solar Cells. *Nano Lett.* **2009**, *9*, 2946−2952.
(38) Lombardo, C. J.; Glaz, M. S.; Ooi, Z.-E.; Vanden Bout, D. A.; Dodabalapur, A. Scanning Photocurrent Microscopy of Lateral Organic Bulk Heterojunctions. *Phys. Chem. Chem. Phys.* **2012**, *14*, 13199−13203.
(39) Gao, Y.; Martin, T. P.; Niles, E. T.; Wise, A. J.; Thomas, A. K.; Grey, J. K. Understanding Morphology-Dependent Polymer Aggregation Properties and Photocurrent Generation in Polythiophene/Fullerene Solar Cells of Variable Compositions. *J. Phys. Chem. C* **2010**, *114*, 15121−15128.
(40) Collins, B. A.; Li, Z.; Tumbleston, J. R.; Gann, E.; McNeill, C. R.; Ade, H. Absolute Measurement of Domain Composition and Nanoscale Size Distribution Explains Performance in Ptb7:Pc71bm Solar Cells. *Adv. Energy Mater.* **2013**, *3*, 65−74.
(41) Hammond, M. R.; Kline, R. J.; Herzing, A. A.; Richter, L. J.; Germack, D. S.; Ro, H.-W.; Soles, C. L.; Fischer, D. A.; Xu, T.; Yu, L.; et al. Molecular Order in High-Efficiency Polymer/Fullerene Bulk Heterojunction Solar Cells. *ACS Nano* **2011**, *5*, 8248−8257.
(42) Ostrowski, D. P.; Vanden Bout, D. A. Correlation of Morphology with Photocurrent Generation in a Polymer Blend Photovoltaic Device. *Small* **2014**, *10*, 1821−1829.
(43) Guide, M.; Dang, X.-D.; Nguyen, T.-Q. Nanoscale Characterization of Tetrabenzoporphyrin and Fullerene-Based Solar Cells by Photoconductive Atomic Force Microscopy. *Adv. Mater. (Weinheim, Ger.)* **2011**, *23*, 2313−2319.
(44) Vanecek, M.; Poruba, A. Fourier Transform Photocurrent Spectroscopy Applied to a Broad Variety of Electronically Active Thin Films (Silicon, Carbon, Organics). *Thin Solid Films* **2007**, *515*, 7499−7503.
(45) Shao, G.; Rayermann, G. E.; Smith, E. M.; Ginger, D. S. Morphology-Dependent Trap Formation in Bulk Heterojunction Photodiodes. *J. Phys. Chem. B* **2013**, *117*, 4654−4660.
(46) Cherniavskaya, O.; Chen, L.; Weng, V.; Yuditsky, L.; Brus, L. E. Quantitative Noncontact Electrostatic Force Imaging of Nanocrystal Polarizability. *J. Phys. Chem. B* **2003**, *107*, 1525−1531.
(47) Silveira, W. R.; Marohn, J. A. Microscopic View of Charge Injection in an Organic Semiconductor. *Phys. Rev. Lett.* **2004**, *93*, 116104.
(48) Kaake, L. G.; Jasieniak, J. J.; Bakus, R. C.; Welch, G. C.; Moses, D.; Bazan, G. C.; Heeger, A. J. Photoinduced Charge Generation in a

DOI: 10.1021/acs.jpclett.5b01360
J. Phys. Chem. Lett. 2015, 6, 2852−2858

Molecular Bulk Heterojunction Material. *J. Am. Chem. Soc.* **2012**, *134*, 19828−19838.
(49) Martens, T.; D'Haen, J.; Munters, T.; Beelen, Z.; Goris, L.; Manca, J.; D'Olieslaeger, M.; Vanderzande, D.; De Schepper, L.; Andriessen, R. Disclosure of the Nanostructure of Mdmo-Ppv:Pcbm Bulk Hetero-Junction Organic Solar Cells by a Combination of Spm and Tem. *Synth. Met.* **2003**, *138*, 243−247.
(50) Krauss, T. D.; Brus, L. E. Charge, Polarizability, and Photoionization of Single Semiconductor Nanocrystals. *Phys. Rev. Lett.* **1999**, *83*, 4840−4843.
(51) Shaheen, S. E.; Brabec, C. J.; Sariciftci, N. S.; Padinger, F.; Fromherz, T.; Hummelen, J. C. 2.5% Efficient Organic Plastic Solar Cells. *Appl. Phys. Lett.* **2001**, *78*, 841−843.
(52) Hoppe, H.; Niggemann, M.; Winder, C.; Kraut, J.; Hiesgen, R.; Hinsch, A.; Meissner, D.; Sariciftci, N. S. Nanoscale Morphology of Conjugated Polymer/Fullerene-Based Bulk- Heterojunction Solar Cells. *Adv. Funct. Mater.* **2004**, *14*, 1005−1011.
(53) Wise, A. J.; Precit, M. R.; Papp, A. M.; Grey, J. K. Effect of Fullerene Intercalation on the Conformation and Packing of Poly-(2-Methoxy-5-(3′-7′-Dimethyloctyloxy)-1,4-Phenylenevinylene). *ACS Appl. Mater. Interfaces* **2011**, *3*, 3011−3019.
(54) Park, L. Y.; Munro, A. M.; Ginger, D. S. Controlling Film Morphology in Conjugated Polymer:Fullerene Blends with Surface Patterning. *J. Am. Chem. Soc.* **2008**, *130*, 15916−15926.

DOI: 10.1021/acs.jpclett.5b01360
J. Phys. Chem. Lett. 2015, 6, 2852−2858